Title	Demonstration of tomographic imaging of isotope distribution by nuclear resonance fluorescence
Author(s)	Zen, Heishun; Ohgaki, Hideaki; Taira, Yoshitaka; Hayakawa, Takehito; Shizuma, Toshiyuki; Daito, Izuru; Yamazaki, Jun-ichiro; Kii, Toshiteru; Toyokawa, Hiroyuki; Katoh, Masahiro
Citation	AIP Advances (2019), 9(3)
Issue Date	2019-03
URL	http://hdl.handle.net/2433/243832
Right	
Type	Journal Article
Textversion	publisher

Demonstration of tomographic imaging of isotope distribution by nuclear resonance fluorescence

Cite as: AIP Advances 9, 035101 (2019); doi: 10.1063/1.5064866
Submitted: 9 October 2018 • Accepted: 21 February 2019 •
Published Online: 1 March 2019

Heishun Zen,[1,a)] Hideaki Ohgaki,[1] Yoshitaka Taira,[2] Takehito Hayakawa,[3] Toshiyuki Shizuma,[3] Izuru Daito,[1,b)] Jun-ichiro Yamazaki,[4] Toshiteru Kii,[1] Hiroyuki Toyokawa,[2] and Masahiro Katoh[4]

AFFILIATIONS

[1]Institute of Advanced Energy, Kyoto University, Uji, Kyoto 611-0011, Japan
[2]National Institute of Advanced Industrial Science and Technology, Tsukuba, Ibaraki 305-8568, Japan
[3]National Institutes for Quantum and Radiological Science and Technology, Tokai, Ibaraki 319-1106, Japan
[4]Insititute for Molecular Science, National Institutes of Natural Sciences, Okazaki, Aichi 444-8585, Japan

[a)]**Correspondence to** Heishun Zen (zen@iae.kyoto-u.ac.jp).
[b)]**Present address:** Nippon Advanced Technology Co., Ltd., Ibaraki, Osaka 5670031, Japan

ABSTRACT

Computed Tomography (CT) using X-ray attenuation by atomic effects is now widely used for medical diagnosis and industrial non-destructive inspection. In this study, we performed a tomographic imaging of isotope (^{208}Pb) distribution by the Nuclear Resonance Fluorescence (NRF), i.e. isotope specific resonant absorption and scattering of gamma rays, using Laser Compton Scattering (LCS) gamma rays. The NRF-CT image which includes both effects of atomic attenuation and nuclear resonant attenuation was obtained. By accounting for the atomic attenuation measured by a conventional method at the same time, a clear ^{208}Pb isotope CT image was obtained. The contrast degradation due to notch refilling caused by small-angle Compton scattering is discussed. This study clearly demonstrates the capability of the isotope-specific CT imaging based on nuclear resonant attenuation which will be a realistic technique when the next generation of extremely intense LCS gamma-ray sources will be available. The expected image acquisition time using these intense LCS gamma rays was discussed.

INTRODUCTION

Computed Tomography (CT) using X-ray attenuation by atomic interaction has been used in various fields such as medical diagnosis and industrial non-destructive inspection. CT scanning of high density and high-Z industrial object using gamma rays from radioisotopes,[1] Bremsstrahlung gamma rays in the MeV energy region,[2] and quasi-monochromatic gamma rays[3] generated by laser Compton scattering (LCS)[4,5] have been studied.

Previous studies[6,7] have proposed a novel method to measure CT images for high density and high-Z objects based on identification of a specific nuclide with Nuclear Resonance Fluorescence (NRF), which is an interaction between a gamma ray and an atomic nucleus and has been studied for non-destructive analysis in industrial applications.[8–12] Hereafter, we call the CT imaging based on NRF as NRF-CT. If the energy of an incident gamma ray is identical with the energy of an excited level of a nucleus, the gamma ray is effectively absorbed by the nucleus, and subsequently the nucleus predominantly decays out by the emission of a gamma ray. Because the NRF energy is specific to each nuclide, one can selectively measure a nuclide of interest. By measuring the scattered gamma ray having the excitation energy of the nuclide or the absorption of the incident gamma ray, the quantity of the nuclide of interest can be evaluated. The transmitted gamma ray has a sharp dip, called as notch, at the NRF energy due to the resonance absorption of the gamma ray by the nucleus. The notch detection method to measure the depth of the notch in the transmitted energy spectrum through a witness target which consists of the isotope of interest and placed

after the target to be measured has been proposed.[9] In this method, the depth of the notch is evaluated by the amount of NRF gamma ray from the witness target. In the previous numerical study on the NRF-CT, the notch detection method was utilized for measuring the amount of the isotope of interest along the gamma-ray beam path. Moreover, the critical effect to the notch detection method called as notch refilling due to the small-angle Compton scattering[9] and multi-step process[13] has been investigated.

The Laser Compton Scattering (LCS) gamma-ray beam is suitable for gamma-ray sources for the NRF measurements. Quasi-monochromatic gamma rays can be generated by LCS, collision of high energy electron bunches and optical laser beams.[4,5] The LCS gamma ray has several excellent characteristics such as good directivity, quasi-monochromatic energy spectrum, variable energy, controllable polarization and possibility of high flux.

The NRF with LCS gamma-ray beams has been proposed for nondestructive assay of hidden materials.[8–10] Kikuzawa *et al.* performed a proof-of-principle experiment for the NRF nondestructive analysis with LCS gamma-ray beams by measuring a lead block shielded by iron plates with a thickness of 1.5 cm.[11] This method can be extended to the nondestructive analysis of the chemical compounds of hidden materials, which was demonstrated by measuring a chemical compound of melamine hidden by an iron plate with a thickness of 1.5 cm and a lead plate with a thickness of 4 mm.[14]

We have already demonstrated that the NRF-CT can identify the position of the isotope of interest but the quality of the reconstructed images was not enough good to discuss the capability of NRF-CT.[15] In this report, we present the experimental results of the NRF-CT based isotope imaging of a newly designed target with better statistics. We measured a two-dimensional CT image of a lead isotope, ^{208}Pb, inside a sample of an aluminum cylinder including an iron rod, a lead rod, and a vacancy (air). The NRF image directly obtained from the measurements includes both effects of atomic and nuclear resonant attenuation. By accounting for the atomic attenuation measured by a conventional method at the same time, a clear image of ^{208}Pb isotope was measured. The notch refilling effect due to the small-angle Compton scattering in this experiment and possible way to reduce the notch refilling effect was discussed. In addition, the expected required measurement time in the next generation of extremely high flux LCS gamma-ray sources was also discussed in this research since the increase of the gamma-ray flux is the key to reduce the required measurement time in one observation point and to obtain CT images with higher resolution within reasonable measurement time.

METHODS

The experiment was carried out at the UVSOR-III electron storage ring.[16] Figure 1 illustrates the measurement setup of the NRF-CT experiment. An LCS gamma-ray source has been developed at the BL1U of the UVSOR-III electron storage ring.[17] In the present experiment, the LCS gamma-ray beam with flux of approximately 2 photons/s/eV was provided by LCS of the 1.94-μm wavelength laser with 746-MeV energy electrons. The maximum energy of the LCS gamma-ray beam was 5403 ± 16 keV. The diameter of the gamma-ray beam on the CT target was 8 mm, which was determined by the collimator. The LCS gamma-ray spectrum on the CT target after the collimator was calculated by the EGS5 code[18] [see the dashed line in Fig. 2(a)]. The energy width of the LCS gamma ray was approximately 1.5 MeV.

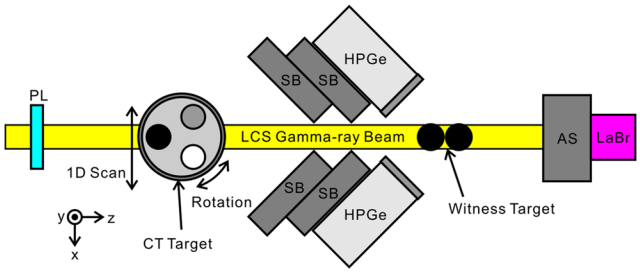

FIG. 1. Schematic illustration of the NRF-CT experimental setup. The incident gamma ray was measured by a plastic scintillation detector (PL) and the transmitted gamma ray was measured by a $LaBr_3$(Ce) detector (LaBr). The scattered gamma rays from the witness target were measured by the two HPGe detectors. Shielding blocks (SB) were used to prevent the directly scattered gamma ray enter to the HPGe detectors. An absorber (AS) was arranged in front of $LaBr_3$(Ce) detector to avoid the saturation of $LaBr_3$(Ce) detector.

As illustrated in Fig. 1, a plastic scintillation detector, a CT sample target, a witness target, and a $LaBr_3$(Ce) detector were arranged on the gamma-ray beam path. The flux of the transmitted gamma rays was measured by the $LaBr_3$(Ce) detector to evaluate the atomic attenuation. The incident gamma-ray flux was measured by the plastic scintillator. The gamma rays scattered from the witness target by NRF were measured by two high purity germanium (HPGe) detectors to evaluate the nuclear resonant attenuation by a specific isotope using the notch detection method.[9] The incident gamma rays with energies of resonances in the nuclide of interest in the CT target are resonantly attenuated. This attenuation makes a notch in the transmitted gamma-ray spectrum. The transmitted gamma rays are subsequently injected to the witness target made of the nuclide to be measured. In the witness target, the gamma rays with energy of the NRF level are partly scattered by NRF. The notch depth can be evaluated from the difference between the NRF yields with and without the CT target. However, these NRF yields depend on both the atomic attenuation and the resonant attenuation in the CT target. The resonant attenuation can be obtained by accounting for the atomic attenuation measured by the $LaBr_3$(Ce) detector from the total attenuation obtained from the NRF yields.

The CT target consisted of an 8-mm diameter natural lead rod, a 10-mm iron rod, and a 10-mm cylindrical air hole implanted in a 30-mm aluminum cylinder wrapped by an iron cylinder with a thickness of 2.5 mm. The aim of this demonstration was to measure the NRF-CT image of the lead using a 5292-keV NRF level of ^{208}Pb. Because the natural abundance of ^{208}Pb is 52.4%, we used two natural lead rods with a diameter of 8 mm as the witness target. The CT target was placed on a three axis movable stage which was able to change the horizontal (x), vertical (y) positions, and rotation angle (θ). The horizontal position (x) was varied from -15 to 15 mm in steps of 5 mm and the rotation angle (θ) was varied from 0 to 150 degree in steps of 30 degree. The gamma-ray spectrum without the CT target was also measured. In total, gamma-ray spectra under the 43 different conditions were measured within 60 hours.

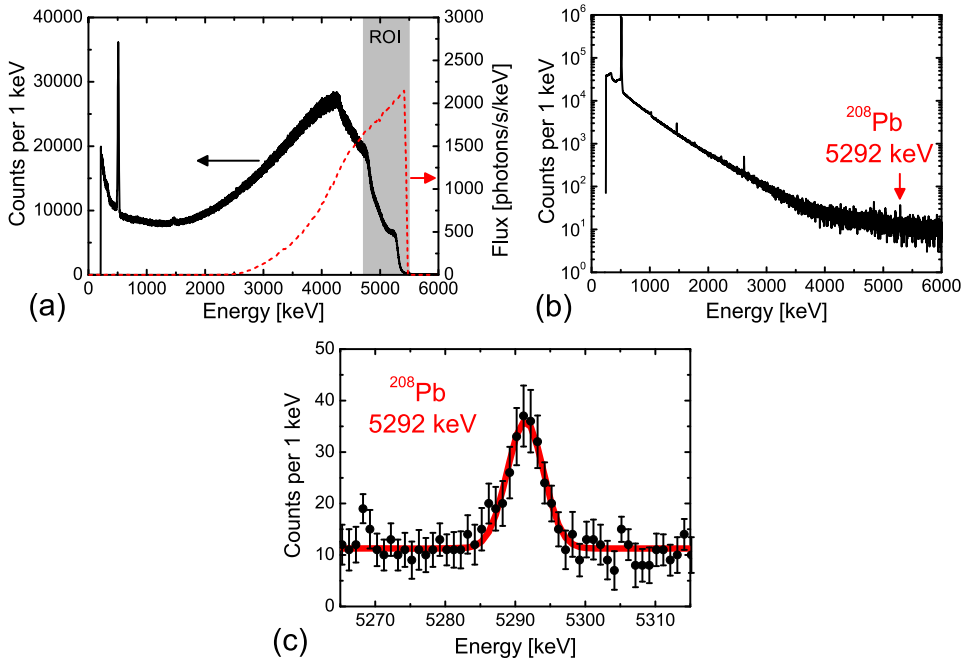

FIG. 2. (a) The solid line shows a typical energy spectrum resulting from measurement of the transmitted gamma rays, which was measured by the $LaBr_3(Ce)$ scintillation detector. The dashed line shows the LCS gamma-ray spectrum after a 8-mm-diameter collimator, which was calculated by the EGS5 code.[18] (b) Typical spectrum of scattered gamma ray from the witness target measured by the HPGe detector. (c) Expanded spectrum around 5292 keV with a Gaussian peak fitting result. The statistical error is shown by the error bar.

The transmission factor of off-resonance gamma rays at the measurement point of a horizontal position x and a rotation angle θ can be given as

$$\varepsilon_{\mathrm{OFF}}(x,\theta) = \exp\left[-\left(\frac{\mu}{\rho}\right)_{\mathrm{ave}}(x,\theta)\cdot\rho_{\mathrm{ave}}(x,\theta)\cdot L\right], \quad (1)$$

where $(\mu/\rho)_{\mathrm{ave}}(x,\theta)$ is the averaged mass attenuation coefficient, $\rho_{\mathrm{ave}}(x,\theta)$ is the average density, and L is the length of the CT target.[19] The solid line in Fig. 2(a) shows a typical energy spectrum measured by the $LaBr_3(Ce)$ detector. The integrated count rate in the energy region from 5500 keV down to its single escape shoulder (ROI) was obtained for each measurement point. Each rate was normalized by the total integrated count rate measured by the plastic scintillation detector. The transmission factor of the CT target at each condition was experimentally obtained as

$$\varepsilon_{\mathrm{OFF}}(x,\theta) = \frac{C_{\mathrm{OFF}}(x,\theta)}{C_{\mathrm{OFF,blank}}}, \quad (2)$$

where $C_{\mathrm{OFF}}(x,\theta)$ is the integrated count rate with the CT target at the measurement of the horizontal position of x and the rotational angle of θ, and $C_{\mathrm{OFF,blank}}$ is the integrated count rate without the CT target. Because the width of ROI is wider than the resonance width of the NRF level by 4-5 orders of magnitudes, the contribution of the resonant attenuation to the integrated count rate is negligibly small. Figures 2(b) and 2(c) show typical gamma-ray spectra measured by the HPGe detectors. The yield of the 5292-keV NRF peak of ^{208}Pb was evaluated by the least square fitting of Gaussian function and normalized by the live time of each measurement. The transmission factor of on-resonance gamma rays can be given as

$$\varepsilon_{\mathrm{ON}}(x,\theta) = \exp\left[-\left(\left(\frac{\mu}{\rho}\right)_{\mathrm{ave}}(x,\theta)\cdot\rho_{\mathrm{ave}}(x,\theta)\cdot L + \sigma_{\mathrm{NRF}}\cdot N_{\mathrm{t}}(x,\theta)\right)\right], \quad (3)$$

where σ_{NRF} is the NRF cross section of the nuclide to be measured, $N_{\mathrm{t}}(x,\theta)$ is the number areal density of the nuclide on the gamma-ray beam path in the CT target.[19] The transmission factor of the CT target at each condition was experimentally obtained as

$$\varepsilon_{\mathrm{ON}}(x,\theta) = \frac{C_{\mathrm{ON}}(x,\theta)}{C_{\mathrm{ON,blank}}}, \quad (4)$$

where $C_{\mathrm{ON}}(x,\theta)$ is the NRF count rate with the CT target, and $C_{\mathrm{ON,blank}}$ is the NRF count rate without the CT target. Finally, the resonant attenuation $-\ln(\varepsilon_{\mathrm{NRF}}(x,\theta))$ was reconstructed from Equations (1)–(4),

$$\begin{aligned} -\ln(\varepsilon_{\mathrm{NRF}}(x,\theta)) &= -[\ln(\varepsilon_{\mathrm{ON}}(x,\theta)) - \ln(\varepsilon_{\mathrm{OFF}}(x,\theta))] \\ &= \sigma_{\mathrm{NRF}}\cdot N_{\mathrm{t}}(x,\theta). \end{aligned} \quad (5)$$

Equation (5) indicates that it is possible to obtain an isotope CT image by subtracting the contribution from the atomic attenuation in logarithmic expression.

There are, in general, two kinds of reconstruction algorithm used for CT: analytical algorithm and iterative algorithm. The analytical algorithm has an advantage that it can be done very fast, but strong noises called as "artifacts" affect the reconstructed image quality if the number of observation angles is few or observation angles are limited by some obstacles. To overcome this limited-angle problem, the iterative algorithms including the Algebraic Reconstruction Techniques (ART) algorithm have been developed.[20-27] For the image reconstruction, the ART algorithm was used in this

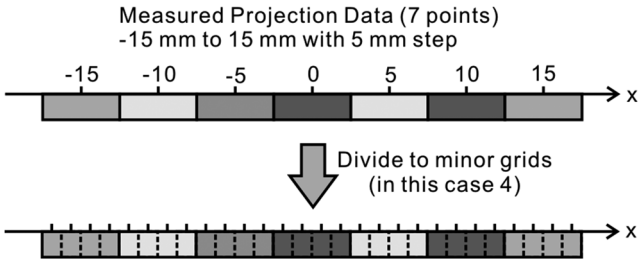

FIG. 3. Schematic image of the division of projection data points to minor grids. The color indicates the attenuation value, which stays constant through the up-sampling step.

study. In the present implementation of the ART algorithm, an initial reconstructed image $\mu_0(x, z)$, which is a two-dimensional matrix, is filled with the value of zero. This initial image is modified to the final image by applying iteratively the following procedure. The k-th image $\mu_k(x, z)$ obtained by the k times iteration is first rotated by the observation angle θ_j as

$$A_{\theta_j,k}(x\cos\theta_j - z\sin\theta_j, x\sin\theta_j + z\cos\theta_j) = \mu_k(x, z). \quad (6)$$

By subtracting the projection of $A_{\theta j,\ k}(x,\ z_i)$ to the x-axis from the data, $p(x, \theta_j)$, measured at observation angle θ_j, the difference matrix $D_{\theta j,k}(x, z)$ is obtained as

$$D_{\theta_j,k}(x, z) = \frac{1}{N}\left\{p(x, \theta_j) - \sum_{i=1}^{N} A_{\theta_j,k}(x, z_i)\right\}, \quad (7)$$

where N is the total number of data points in a single projection data. Here $D_\theta(x, z)$ has no z dependence. The difference matrix $D_{\theta j,k}(x, z)$ is rotated back as

$$D'_{\theta_j,k}(x\cos\theta_j + z\sin\theta_j, -x\sin\theta_j + z\cos\theta_j) = D_{\theta_j,k}(x, z). \quad (8)$$

By adding the summation of the difference matrix, the $(k+1)$-th reconstructed image $\mu_{k+1}(x, z)$ is calculated as

$$\mu_{k+1}(x, z) = \mu_k(x, z) + \frac{\alpha}{M}\sum_{j=1}^{M} D'_{\theta_j,k}(x, z), \quad (9)$$

where α is the relaxation parameter used to control the feedback strength and M is the total number of the observation angles. The relaxation parameter α should be less than unity. In this work, α was set to be 0.7. The convergence of the reconstruction is judged by the root-mean-square-difference (RMSD) between the k and $k+1$ reconstructed images given by

$$\mathrm{RMSD} = \left[\frac{1}{N^2}\sum_{i=1}^{N}\sum_{j=1}^{N}\{\mu_{k+1}(x_i, z_j) - \mu_k(x_i, z_j)\}\right]^{1/2}. \quad (10)$$

When the RMSD get smaller than user specified value, the iteration is stopped. Then the reconstructed distribution $\mu_{k+1}(x, z)$ can be obtained. There are some CT reconstruction algorithms having non-negative constraints which is preferable for NRF-CT since the attenuation is always positive in principle. However, the ART algorithm used in this study doesn't have non-negative constraints. There is room for improvement concerning the algorithm for CT reconstruction.

The developed ART algorithm requires the matrix rotation using the Equations (6) and (8). This matrix rotation is very simple and applicable to any size of reconstruction image or projection data. However, when the number of data points is few as like the present NRF-CT experiment, the accuracy of the matrix rotation becomes low. To mitigate this problem, before reconstruction, we introduced a preprocessing step; we divided each projection data point to minor grids as shown in Fig. 3. In Fig. 3, the color indicates the attenuation value, which stays constant through the up-sampling step.

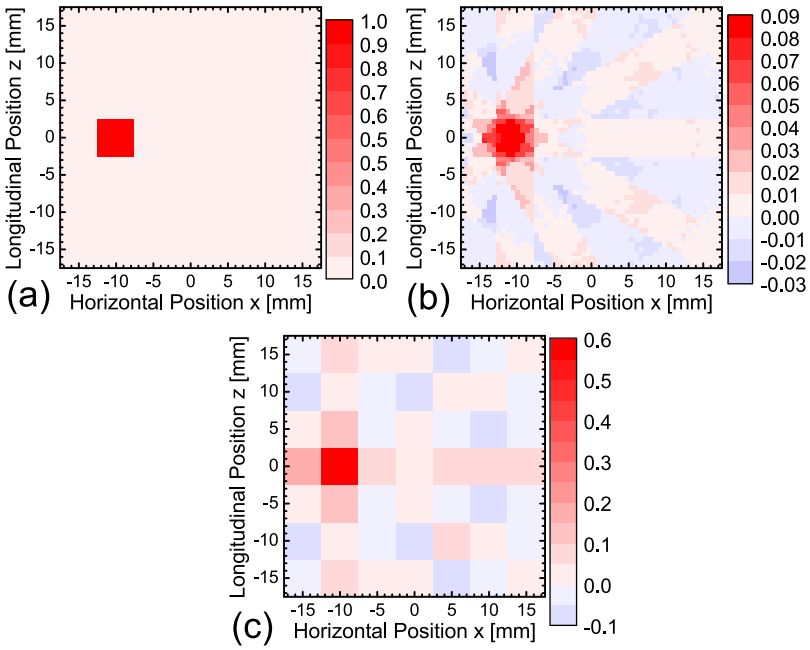

FIG. 4. (a) The original distribution used for the demonstration. (b) The reconstructed image before the post-process step. (c) The reconstructed image after the post-process step.

By this preprocessing step, the density of the grid points was able to be increased and the accuracy of the matrix rotation was able to be improved. In the present study, each projection data point was divided into 8 points having the same value with the original grid point. As a result, the spatial frequency of the data input into the ART reconstruction procedure was artificially increased 8-fold. To get back to the initial resolution after the reconstruction, we implemented a post-process step, in which each 8×8 points in the reconstructed image was merged together. The grid size of the reconstructed image got back to that identical with the original projection data.

We demonstrated the capability of the developed reconstruction procedure using a sample. We assumed that only one point at $(x, z) = (-10, 0)$ was occupied by a high-Z material as shown in Fig. 4(a) and that the condition of projection angle was same with the present experiment, i.e. from 0 to 150 degree with 30 degree interval. The reconstructed image before the post-process step is shown in Fig. 4(b). The reconstructed distribution has weak artifacts in radial pattern. These artifacts are generated due to the small number of the observation angles. The highest signal position in Fig. 4(b) is slightly shifted to the negative horizontal direction. This is because of the insufficient measurement points and the number of observation angles for the increased spatial frequency after the preprocessing step. After the post-process step, the final reconstructed image having same grid size with the original one was obtained as Fig. 4(c). The peak width is slightly wider than the original one and the peak count of the final reconstructed image is not as high as the original one. However, we can clearly find the position of the peak at $(x, z) = (-10, 0)$. The small shift to the negative horizontal direction observed in Fig. 4(b) does not impact the results shown in Fig. 4(c). The integrated count of the reconstructed distribution around the peak (1.1) is almost same with the peak count of the original distribution (1.0). This result shows that the developed procedure can reconstruct the 2D distribution from the low-resolution projection data with the small number of observation angles.

RESULTS

By using the developed reconstruction procedure, we obtained 7×7 images with 5-mm pixel size from the measured gamma-ray spectra. Figure 5(a) is the image of the atomic attenuation distribution obtained by the gamma-ray transmission measured by the $LaBr_3(Ce)$ detector. Although the resolution of the reconstructed image is not high, strong attenuation by the lead rod around $(x, z) = (0, -10)$, medium attenuation by the iron rod around $(x, z) = (-7.5, 5)$, and weak attenuation due to vacancy around (x, z) = (7.5, 5) can be recognized. Figure 5(b) is the distribution of the on-resonance gamma-ray attenuation including the atomic and resonant attenuation. This clearly indicates the distribution of ^{208}Pb located around $(x, z) = (0, -10)$, but the atomic attenuation by the iron rod has still remained. Figure 5(c) is the distribution of the resonant attenuation induced by ^{208}Pb, which was obtained by Equation (5). The contrast of the lead rod against the background is higher than that of Figure 5(b). This result shows that it is practically possible to measure the NRF-CT image by the previously proposed method.[6,7]

As one can see in Figure 5(c), the highest NRF attenuation position measured was (x, z) = (0, -5), which was slightly different from the expected geometric centre of the lead rod (x, z) = (0, -8). In addition, the iron rod can be seen in Figure 5(a) also slightly shifted to positive z direction as same as the lead rod in Figure 5(c). This shift could occur when the misalignment of rotation stage existed or the slight shift of gamma-ray beam path during the long time data acquisition. More precise adjustment and tolerance of misalignment of rotation stage must be investigated for practical applications. Moreover, the way to measure the gamma-ray beam position should be developed to avoid undesired image distortion.

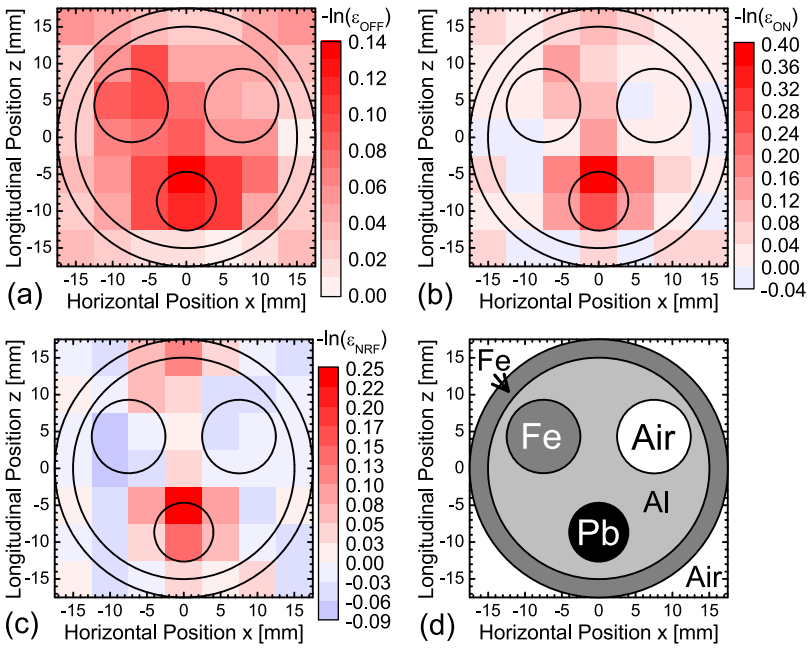

FIG. 5. (a) CT reconstruction result of off-resonance attenuation which is same with normal gamma-ray CT. (b) CT reconstruction result of on-resonance attenuation which include the atomic and nuclear resonant attenuation. (c) CT reconstruction result of nuclear resonant attenuation. (d) Geometry of the CT target.

DISCUSSION

The previous studies[9,28] reported that the small-angle Compton scattering in targets refill the notch induced by NRF attenuation in the sample. Simple numerical calculations were performed to evaluate the notch refilling effect. The amount of the small-angle Compton scattering photon which refill the notch effect, N_{refill} can be calculated by

$$N_{\mathrm{refill}} = \sigma_{\mathrm{e,target}} \int_{E_{\mathrm{res}}}^{E_{\mathrm{max}}} N_{\gamma}(E) \int_{\Omega(\mathrm{E})} \frac{\mathrm{d}\sigma_{\mathrm{C}}}{\mathrm{dE}} d\Omega \, dE, \qquad (11)$$

where $\sigma_{\mathrm{e,target}}$ is the areal density of electron in the target material along the gamma-ray beam path, E_{res} is the NRF resonant energy of the interest, E_{max} is the highest energy should be taken into account, $N_{\gamma}(E)$ is the number of incident gamma-ray photon at the energy E, $\mathrm{d}\sigma_{\mathrm{C}}/\mathrm{d}\Omega$ is the differential cross section of the small-angle Compton scattering. In the case of small-angle Compton scattering with scattering angle of less than 0.1 rad, the differential cross section $\mathrm{d}\sigma_{\mathrm{C}}/\mathrm{d}\Omega$ is almost constant (around 8×10^{-26} $\mathrm{cm^{-2}sr^{-1}electron^{-1}}$) and has almost no dependence on the energy and polarization angle of the gamma ray (more detailed information is described in supplementary material available online). After the small-angle Compton scattering, quite small fraction of the gamma-ray photon which initially has higher energy than the NRF resonant energy can be scattered to the NRF resonant energy and refill the notch created by the NRF in the CT target. The scattering angle θ_{s}, incident gamma-ray photon energy E_0 and scattered gamma-ray photon energy E_1 has the relationship which can be described as[29]

$$\theta_{\mathrm{s}} = \cos^{-1}\left[1 - \frac{m_0 c^2}{E_0}\left(\frac{E_0}{E_1} - 1\right)\right], \qquad (12)$$

where m_0 is the electron rest mass and c is the velocity of light. When the incident gamma-ray photon energy and the scattered gamma-ray photon energy are given, the scattering angle of the gamma ray is uniquely determined. Therefore, E_{max} in the Equation (11) depends on the geometrical configuration of the witness target. The integration of Equation (11) with taking into account the experimental geometry was performed (more detailed information is described in supplementary material available online). As the result, the reduction of the notch effect evaluated by numerical calculation is less than 0.1% in the present experiment. The reduction of the notch effect can be reduced down to 0.01% by using the witness target which has the same transverse size with the gamma-ray beam. The corresponding degradation of attenuation amounts $\Delta[-\ln(\varepsilon_{\mathrm{NRF}})]$ for the present experiment and the optimized configuration are -4×10^{-4} and -4×10^{-5}, respectively. Those values are negligibly small compared with the obtained attenuation amount (around 0.2, shown in Fig. 5(c)). The differential cross section of the small-angle Compton scattering was calculated based on the photon scattering by free electrons at rest, although the electrons in the CT target are bound atomic electrons. It is known that the differential cross section of the Compton scattering by the bound atomic electrons is almost the same as that by the free electrons when the quantity x_{c} $(= \sin(\theta_{\mathrm{S}}/2)/\lambda_0[\mathrm{Å}] = 12.4 \sin(\theta_{\mathrm{S}}/2)\, E_0[\mathrm{keV}])$ is larger than 10, where λ_0 is the wavelength of the incident gamma ray.[30] Therefore, the Compton scattering by free electrons is a good approximation in the present case, i.e. $x_{\mathrm{c}} \approx 5000$ for $E_0 = 5300$ keV and $\theta_{\mathrm{S}} = 0.06$ rad.

In the present demonstration, we only obtained the low resolution image of 7×7 with the gamma-ray beam with flux of 2 photons/s/eV and measurement time of 60 hours. The required measurement time is inversely proportional to gamma-ray flux. The next generation of extremely high flux LCS gamma-ray sources, ELI-NP-GBS,[31] MEGa-ray,[32] and HIγS2,[33] have been constructed or proposed. Although optimization of the collimator size and the detector arrangement will be required, when the ELI-NP-GBS[31] with flux of 5000 photons/s/eV becomes available in the near future, the required data accumulation time at a single observation condition can be 2500 shorter than this experiment. This means we can obtain 100 times as many CT measurement points within 3 hours. Since the spatial resolution of the reconstructed CT image is determined by the scanning interval, the number of rotation angle, and the incident beam width, the expected reconstructed CT image can be 10 times improved. However, the geometry of the detector system has to be considered to take into account the maximum counting rage of the detectors.

One of excellent advantages of NRF-CT is that it is possible to distinguish an element of interest from other elements even if both elements have similar atomic numbers, such as a combination of iron (Z=26) and nickel (Z=28), and tantalum (Z=73) and tungsten (Z=74). Moreover, this method can be applied to measurement of a specific isotope of the same element such as ^{235}U inside uranium. Finally, we would like to point out that we can measure CT images of several different nuclides at the same time using wideband[14] or multi-colour LCS gamma-ray beam.[34]

CONCLUSION

We have shown that the NRF-CT technique can enable us to get a tomographic image of isotope (^{208}Pb) in a natural lead rod concealed inside in an iron cylinder filled with aluminium together with an iron rod. In the reconstructed isotope image and the atomic attenuation CT image, slight shift (around 3 mm) in one direction from the expected position was observed. This shift is possibly caused by the misalignment of the rotation stage or the shift of the gamma-ray beam path during the long time experiment. This implies the need of further study and development for practical application of NRF-CT technique. The effect of small-angle Compton scattering in this work was discussed and the corresponding degradation of the attenuation amounts were evaluated to be less than -4×10^{-4} which is negligibly small compared with the obtained attenuation amount, around 0.2. In addition, the required acquisition time in the upcoming high intensity gamma-ray sources were evaluated to be 3 hours for 10 times higher resolution than the present image.

SUPPLEMENTARY MATERIAL

See supplementary material for the detail of calculation of the notch refilling effect induced by the small-angle Compton scattering.

ACKNOWLEDGMENTS

This work was supported by JSPS KAKENHI Grant Number JP18H01916 and JP18H03715, and Joint Research by Institute for Molecular Science (IMS program number 212 in 2015 and 209 in 2016).

REFERENCES

[1] J. Kim, S. Jung, J. Moon, T. Kwon, and G. Cho, Progress in Nuclear Science and Technology **1**, 263 (2011).
[2] N. Estre, D. Eck, J. L. Pettier, E. Payan, C. Roure, and E. Simon, IEEE Trans. Nucl. Sci. **62**, 3104 (2015).
[3] H. Toyokawa, H. Ohgaki, T. Mikado, and K. Tamada, Rev. Sci. Instrum. **73**, 3358 (2002).
[4] R. H. Milburn, Phys. Rev. Lett. **10**, 75 (1963).
[5] F. R. Arutyunian and V. A. Tumanian, Phys. Lett. **4**, 176 (1963).
[6] W. Bertozzi, and R. J. Ledoux, U.S. Patent 8180019 B2 (2012).
[7] C. P. Barty, F. Albert, S. G. Anderson, P. Armstrong, A. Bayramian, G. Beer, R. Cross, C. A. Ebbers, G. Deis, D. J. Gibson, J. Hall, F. V. Hartemann, T. Houck, R. A. Marsh, M. J. Messerly, H. Phan, V. A. Semenov, and S. S. Wu, LLNL-CONF-515893 (2011).
[8] W. Bertozzi and R. J. Ledoux, Nucl. Instrum. Methods Phys. Res. B **241**, 820 (2005).
[9] J. Pruet, D. P. McNabb, C. A. Hagmann, F. V. Hartemann, and C. Barty, J. Appl. Phys. **99**, 123102 (2006).
[10] R. Hajima, T. Hayakawa, N. Kikuzawa, and E. Minehara, J. Nucl. Sci. Technol. **45**, 441 (2008).
[11] N. Kikuzawa, R. Hajima, N. Nishimori, E. Minehara, T. Hayakawa, T. Shizuma, H. Toyokawa, and H. Ohgaki, Appl. Phys. Express **2**, 036502 (2009).
[12] B. J. Quiter, B. A. Ludewigt, V. V. Mozin, C. Wilson, and S. Korbly, Nucl. Instrum. Methods Phys. Res. B **269**, 1130 (2011).
[13] C. Hagmann and J. Pruet, Nucl. Instrum. Methods Phys. Res. B **259**, 895–908 (2007).
[14] T. Hayakawa, H. Ohgaki, T. Shizuma, R. Hajima, and N. Kikuzawa, Rev. Sci. Instrum. **80**, 045110 (2009).
[15] H. Ohgaki, T. Kii, H. Zen, I. Daito, H. Toyokawa, Y. Taira, T. Hayakawa, M. Katoh, and J. Yamazaki, Proceedings of IPAC2016, 2007 (2016).
[16] M. Adachi, H. Zen, T. Konomi, J. Yamazaki, K. Hayashi, and M. Katoh, J. Phys. Conf. Ser. **425**, 042013 (2013).
[17] H. Zen, Y. Taira, T. Konomi, T. Hayakawa, T. Shizuma, J. Yamazaki, T. Kii, H. Toyokawa, M. Katoh, and H. Ohgaki, Energy Procedia **89**, 335 (2016).
[18] H. Hirayama, Y. Namito, A. F. Bielajew, S. J. Wilderman, and W. R. Nelson, SLAC Report number: SLAC-R-730 and KEK Report number: 2005-8 (2015).
[19] I. Daito, H. Ohgaki, G. Suliman, V. Iancu, C. A. Ur, and M. Iovea, Energy Procedia **89**, 389–394 (2016).
[20] R. Gordon, R. Bender, and G. T. Herman, J. Theor. Biol. **29**, 471 (1970).
[21] T. Sato, S. J. Norton, M. Linzer, O. Ikeda, and M. Hirama, Appl. Opt. **20**, 395 (1981).
[22] M. Nassi, W. R. Brody, B. P. Medoff, and A. Macovski, IEEE Transactions on biomedical engineering **29**, 333 (1982).
[23] B. P. Medoff, W. R. Brody, M. Nassi, and A. Macovski, J. Opt. Soc. Am. **73**, 1493 (1983).
[24] K. M. Hanson and G. W. Wecksung, J. Opt. Soc. Am. **73**, 1501 (1983).
[25] J. H. Kim, K. Y. Kwak, S. B. Park, and Z. H. Cho, IEEE Trans. Med. Imaging **4**, 139 (1985).
[26] A. H. Andersen, IEEE Trans. Med. Imaging **8**, 50 (1989).
[27] J. Nuyts, B. D. Man, J. A. Fessler, W. Zbijewski, and F. J. Beekman, Phys. Med. Biol. **58**, R63 (2013).
[28] C. A. Hagmann, J. M. Hall, M. S. Johnson, D. P. McNabb, J. H. Kelley, C. Huibregtse, E. Kwan, G. Rusev, and A. P. Tonchev, J. Appl. Phys. **106**, 084901 (2009).
[29] A. H. Compton, Phys. Rev. **21**, 483 (1923).
[30] J. H. Hubbell, Wm. J. Veigele, E. A. Briggs, R. T. Brown, D. T. Cromer, and R. J. Howerton, J. Phys. Chem. Ref. Data **4**, 471 (1975).
[31] K. Dupraz, K. Cassou, N. Delerue, P. Fichot, A. Martens, A. Stocchi, A. Variola, F. Zomer, A. Courjaud, E. Mottay, F. Druon, G. Gatti, A. Ghigo, T. Hovsepian, J. Y. Riou, F. Wang, A. C. Mueller, L. Palumbo, L. Serafini, and P. Tomassini, Phy. Rev. ST AB **17**, 033501 (2014).
[32] D. J. Gibson, F. Albert, S. G. Anderson, S. M. Betts, M. J. Messerly, H. H. Phan, V. A. Semenov, M. Y. Shverdin, A. M. Tremaine, F. V. Hartemann, C. W. Siders, D. P. McNabb, and C. P. J. Barty, Phy. Rev. ST AB **13**, 070703 (2010).
[33] http://www.tunl.duke.edu/higs2.php.
[34] H. Toyokawa, T. Hayakawa, T. Shizuma, R. Hajima, K. Masuda, and H. Ohgaki, Nucl. Instrum. Methods Phys. Res. A **652**, 21 (2011).